

# Ultra-rapid preparation of large-area high-crystallinity covalent organic framework membranes

Received: 12 July 2025

Accepted: 3 December 2025

Published online: 12 December 2025

Check for updates

Yan Pan<sup>1</sup>, Gangqiang Yu<sup>2</sup>, Luteng Gao<sup>1</sup>, Xueyong Li<sup>1</sup>, Lan Yang<sup>1</sup>, Haiqi Gao<sup>1</sup>, Tianfu Wang<sup>3</sup>, Wenhai Zhang<sup>1</sup>✉, Shengqian Ma<sup>4</sup>✉ & Hong Meng<sup>1</sup>✉

It has been challenging to rapidly prepare high-crystallinity covalent organic framework (COF) membranes particularly in large areas because their crystallization often requires extensive time spent on trial and error and screening. Here, we have developed a reverse-phase microemulsion interfacial polymerization to ultra-rapidly prepare COF membranes in tens of seconds. By creating a special ionic liquid/acetic acid aqueous microemulsion, where the reactive monomers are orderly prearranged within the ionic liquid network, the polymerization and crystallization can concurrently proceed at the phase interface under confined spatial conditions. Meanwhile, the water by-products are promptly encapsulated by the reverse-phase microemulsion, significantly accelerating the polymerization reaction. Using the scraping-assisted process, a large-area high-crystallinity TbPa-COF composite membrane (0.4 × 1.0 m) has been successfully prepared, and the TbPa-COF membrane exhibits high permeability (111.3 L m<sup>2</sup> h<sup>-1</sup> bar<sup>-1</sup>), achieving a bioprotein desalination rate of up to 98% after six cycles, outperforming commercial benchmark membranes (82%). Therefore, through systematic investigation of the ultra-rapid growth mechanism of COF membranes, our work represents a significant milestone for advancing large-area highly crystalline COF membranes for use in practice.

Covalent organic framework (COF) membranes show great potential for diverse applications including molecular separation<sup>1,2</sup>, catalysis<sup>3,4</sup>, optoelectronics<sup>5-7</sup>, and energy storage<sup>8-10</sup>. This potential stems from the porous and conjugated crystal structure of COFs. It is well-known that the COF crystallinity is crucial for advancing their performance<sup>11</sup>. However, COF crystallization often requires extensive time spent on trial and error and screening<sup>12,13</sup>, and the scale-up of high-crystallinity COF membranes poses a significant challenge<sup>14,15</sup>. Consequently, it is urgent to develop a fast process for obtaining large-area high-crystallinity COF membranes.

Improving the production efficiency of large-area COF membranes represents a core challenge in balancing economic feasibility

with process compatibility. The key to achieving this objective lies in accelerating the rates of both reaction and crystallization processes. Although recent advancements in catalyst selection and optimization of the reaction environment (e.g., solvent, temperature) have successfully reduced the crystallization time from days to tens of minutes<sup>16-24</sup>, the overall reaction efficiency remains somewhat inadequate. It is difficult to further shorten the crystallization time based on the conventional mechanism of trial and error and screening<sup>25,26</sup>.

Here, we have developed a simultaneous polymerization and crystallization method that enables the rapid preparation of high-crystallinity COF membranes in mere tens of seconds. We constructed a reverse-phase microemulsion system with an ionic liquid (IL)/acetic

<sup>1</sup>State Key Laboratory of Chemistry and Utilization of Carbon Based Energy Resources, College of Chemistry, Xinjiang University, Urumqi, PR China. <sup>2</sup>College of Environmental Science and Engineering, Beijing University of Technology, Beijing, PR China. <sup>3</sup>School of Environmental Science and Engineering, Frontiers Science Center for Transformative Molecules, Shanghai Jiao Tong University, Shanghai, PR China. <sup>4</sup>Department of Chemistry, University of North Texas, Denton, TX, USA. ✉e-mail: [whzhang@xju.edu.cn](mailto:whzhang@xju.edu.cn); [Shengqian.ma@unt.edu](mailto:Shengqian.ma@unt.edu); [menghong@xju.edu.cn](mailto:menghong@xju.edu.cn)

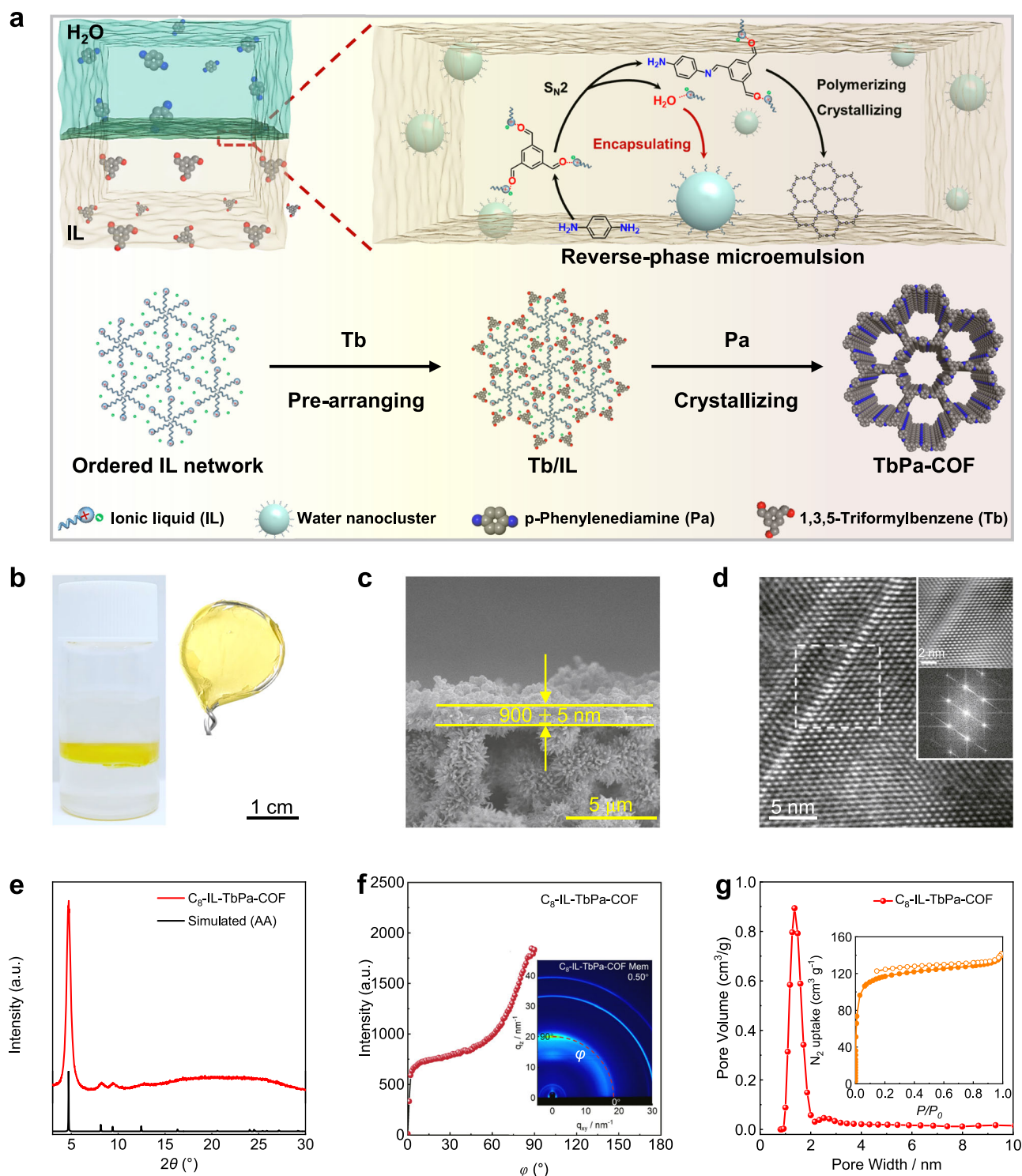


**Fig. 1 | Preparation of  $C_8$ -IL-TbPa-COF membrane with crystallinity and porosity.** **a** Schematic view of the current strategy, which utilizes a reverse-phase microemulsion interface via IL and AcOH aqueous. **b** Digital photographs of the IL/AcOH aqueous reverse-phase microemulsion interface used for preparing the  $C_8$ -IL-TbPa-COF membrane (left) and the resulting  $C_8$ -IL-TbPa-COF membrane (right). **c** Cross-sectional SEM images of the  $C_8$ -IL-TbPa-COF membrane. **d** HRTEM image of the  $C_8$ -IL-TbPa-COF membrane. Insets show the fast Fourier transform (FFT) pattern taken from the regions highlighted by the dashed-line squares and the

corresponding filtered inverse FFT image. **e** Simulated and experimental PXRD patterns for  $C_8$ -IL-TbPa-COF membrane. **f** GIWAXS of  $C_8$ -IL-TbPa-COF membrane with face-on orientations. GIWAXS images obtained at grazing angle of  $0.50^\circ$  for face-on (inset) and  $\varphi$ -dependent orientation distribution function of the (001) facet. The synchrotron GIWAXS patterns data were collected at beamline 19B2 in SPring-8, Japan ( $\lambda = 1.00 \text{ \AA}$ ). **g** Pore size distribution with the corresponding  $N_2$  adsorption isotherms (inset) of the  $C_8$ -IL-TbPa-COF membrane.

acid (AcOH) aqueous interface (Fig. 1a). Because of the strong interaction between the imidazole group of the IL and water molecules, a reverse-phase microemulsion is spontaneously formed. In this case, the continuous phase is the IL while the dispersion phase is AcOH

aqueous. The 1,3,5-triformylbenzene (Tb) monomers are orderly prearranged within the ionic- and hydrogen-bond (ion-HB) network of the hydrophobic IL. After *p*-phenylenediamine (Pa) monomers diffuse from the aqueous phase into the IL phase and contact the prearranged

Tb monomers, the polymerization and crystallization occur simultaneously at the phase interface, which imparts a spatial confinement on the reaction. Meanwhile, water by-products are promptly encapsulated by the reverse-phase microemulsion, significantly accelerating the polymerization reaction.

## Results

### Ultra-rapid fabrication and structural control of COF membranes

A yellow COF membrane is prepared within 30 seconds using 1-octyl-3-methylimidazolium bis((trifluoromethyl) sulfonyl) imide ( $[C_8MIm][NTf_2]$ ) ( $C_8$ -IL) and 60% AcOH aqueous (Fig. 1b, Supplementary Movie 1, Supplementary Figs. 1 and 2), named  $C_8$ -IL-TbPa-COF. Scanning electron microscopy (SEM) images show a surface of nanoparticle accumulation (Supplementary Fig. 3) with a thickness of approximately  $900 \pm 5$  nm (Fig. 1c). The discontinuous packed nanoparticles on the membrane surface are nanoscale COF crystals formed due to interfacial diffusion limitation (Fig. 1c and Supplementary Fig. 4). High-resolution transmission electron microscopy (HRTEM) analysis confirms the COF membrane's clear lattice structures, with a lattice spacing of approximately 0.35 nm, which is consistent with the expected  $d_{001}$  spacing (Fig. 1d). The crystal structures of the  $C_8$ -IL-TbPa-COF membrane were thoroughly analyzed using powder X-ray diffraction (PXRD) and grazing incidence wide-angle X-ray scattering analysis (GIWAXS). The PXRD spectrum reveals a prominent peak at  $2\theta = 4.7^\circ$ , which corresponds to the (100) crystal plane of the COF, indicating the membrane's crystalline nature (Fig. 1e). GIWAXS analysis reveals that  $C_8$ -IL-TbPa-COF is oriented along the (001) crystal plane (Fig. 1f and Supplementary Fig. 5), which may benefit from the ordered prearrangement of monomers and interfacial confined growth (Supplementary Fig. 6). Moreover, Brunauer–Emmett–Teller (Fig. 1g) analysis reveals a specific surface area of  $379 \text{ m}^2 \text{ g}^{-1}$  and predominant pore sizes is 1.4 nm, consistent with the reported TbPa-COF pore structure<sup>27</sup>. These findings collectively affirm the structural crystallinity and porosity of the  $C_8$ -IL-TbPa-COF membrane.

Studies were conducted on the influence of AcOH concentration and the length of IL hydrophobic chain on membrane formation. Increasing the amount of AcOH results in shorter COF crystallization and membrane formation times (Fig. 2a and Supplementary Fig. 7), which could be ascribed to enhanced Brønsted acid catalysis. However, when the AcOH concentration exceeds 60 wt%, the IL/AcOH aqueous interface is unstable (Supplementary Fig. 8). Thus, we used 60 wt% AcOH to investigate the relationship between different carbon chain lengths of IL and the crystallization time of the COF membrane. All six IL ( $C_n$ -IL,  $n = 2, 4, 6, 8, 10, 12$ ) formed stable and clear interfaces with the 60 wt% AcOH aqueous (Supplementary Figs. 9 and 10). When the IL carbon chain length was 6 or fewer, high-crystallinity COF membranes could be prepared within 10 s. For carbon chain lengths up to 8, membrane formation was complete within 30 s. However, with carbon chain lengths exceeding 10, the crystallization time increased slightly because the higher viscosity of ILs with longer carbon chains hindered monomer diffusion and consequently slowed the interfacial polymerization rate (Fig. 2b, Supplementary Figs. 11–13). Furthermore, as the alkyl chain length of IL increases, the prepared COF membrane transforms from loosely packed particles to a more continuous and thinner membrane structure, which is mainly regulated by IL viscosity and water absorption properties on interfacial reaction kinetics and interfacial layer thickness (Supplementary Figs. 14–16). Under the condition of a fixed reaction time of 60 s, comparing the minimum AcOH concentration thresholds required for preparing TbPa-COF membranes in IL systems with different alkyl chain lengths further indicates that IL viscosity is the key parameter determining the reaction kinetics at the IL/AcOH aqueous interface (Supplementary Figs. 17–18). Compared to the crystallization times of COF membranes reported in previous studies (see Fig. 2c and Supplementary Table 1),

the strategy we demonstrate can shorten the membrane preparation dramatically. We also applied our strategy to prepare  $C_8$ -IL-TbBd-COF,  $C_8$ -IL-TbTAPB-COF, and  $C_8$ -IL-TbTTA-COF membranes<sup>28</sup>, all of which were achieved with high-crystallinity within seconds (Fig. 2d–f and Supplementary Figs. 19–23), demonstrating the general applicability of the reverse-phase microemulsion.

### The mechanism of ultrafast COF membrane formation

To gain a deeper understanding of the ultrafast mechanism, we performed experimental studies, Density Functional Theory (DFT) calculations, and molecular dynamics (MD) simulations. It is well known that ILs have ordered network structures due to their ion-HB networks<sup>29</sup>. We found that Tb monomer molecules can be easily embedded in the ion-HB network to prearrange ordered within a confined space due to the monomers' small size and strong hydrogen bonding interaction. This has been confirmed by WAXS (Fig. 3a and Supplementary Fig. 24), radial distribution functions and spatial distribution functions (Fig. 3b and Supplementary Figs. 25–27). The hydrogen bonding interaction between IL and Tb is clearly observed in the Fourier-transform infrared (FT-IR) spectra (Fig. 3c and Supplementary Fig. 28). The order of ILs and the prearrangement of monomers effectively lower the crystallization energy barrier<sup>30–32</sup>. When the temperature increases, the IL order is destroyed, and the obtained membranes are thereby amorphous (Supplementary Fig. 29), which suggests that the IL order is crucial to the formation of high-crystallinity COF membranes.

Moreover, the condensation reaction of aldehyde and amine is a reversible process. Rapid removal of water by-products promotes the forward reaction. In the IL/AcOH aqueous interface, a spontaneously formed reverse-phase microemulsion promptly encapsulates water molecules, leading to a significant enhancement in the polymerization rate kinetics (Fig. 3d and Supplementary Figs. 30–32). By contrast, the IL/p-toluenesulfonic acid (PTSA) aqueous solution system fails to form a reverse-phase microemulsion interface, resulting in the inability to form membrane structures within the 60-second interfacial reaction time. Therefore, the reverse-phase microemulsion interface constructed by AcOH is the key to achieving the ultra-fast synthesis of COF membranes within tens of seconds in this study (Supplementary Figs. 33–34). Additionally, imidazolium-based ILs exhibit strong Lewis acidity, effectively activating aldehyde groups and reducing the activation energy barrier for Schiff base reaction, thus thermodynamically promoting the reaction rate<sup>33</sup>. DFT calculations demonstrate that the binding energy between Tb and Pa significantly increases from  $-16.5 \text{ kJ/mol}$  to  $-95.2 \text{ kJ/mol}$  in  $C_8$ -IL (Fig. 3e and Supplementary Fig. 35). Meanwhile, ILs exhibit good solubility for Tb monomer molecules, thereby achieving a high concentration of monomers and thus accelerating polymerization. Therefore, the reverse-phase microemulsion system achieves a synergistic enhancement of thermodynamics and kinetics under confined spatial conditions, ultimately enabling the rapid preparation of high-crystallinity COF membranes.

### Scaling-up and application of COF composite membrane

We have successfully adopted reverse-phase microemulsion interfacial polymerization to prepare a large-area high-crystallinity  $C_8$ -IL-TbPa-COF composite membrane ( $0.4 \times 1.0 \text{ m}$ ) using a scraping-assisted process<sup>34</sup> (Fig. 4a). X-ray Photoelectron Spectroscopy (XPS) results indicate that the IL on the TbPa-COF composite membrane was completely removed (Supplementary Fig. 36). SEM images reveal that the  $C_8$ -IL-TbPa-COF separation layer was continuous with a thickness of approximately  $115 \pm 5$  nm (Supplementary Fig. 37). Notably, the thickness of COF membranes prepared via traditional interfacial polymerization ( $900 \pm 5$  nm) is approximately 7.5 times that of those fabricated by the SAIP method ( $115 \pm 5$  nm). This significant difference arises from the restricted diffusion of monomers by the PAN substrate (Supplementary Fig. 38), which hinders excessive thickness growth,

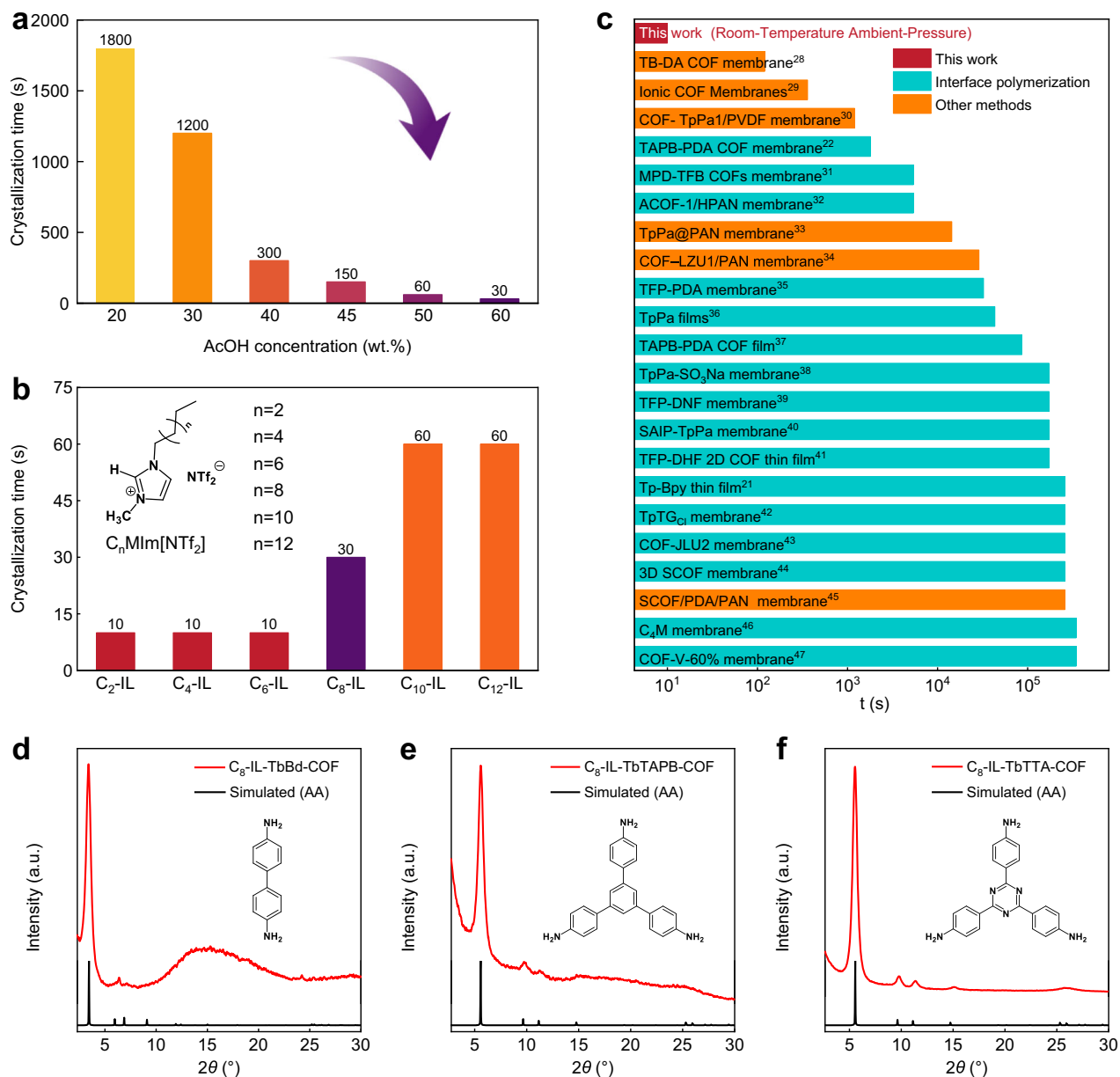


**Fig. 2 | Second-scale preparation of COF membranes.** **a** Relationship between AcOH concentration and the minimum time required for crystallization of TbPa-COF membranes at the C<sub>8</sub>-IL/AcOH aqueous reverse-phase microemulsion interface. **b** Comparison of the minimum crystallization time for TbPa-COF membranes prepared by the reverse-phase microemulsion interfacial polymerization in C<sub>n</sub>-IL

( $n = 2, 4, 6, 8, 10, 12$ )/60 wt% AcOH aqueous. **c** Our preparation of COF membranes compared to literature COF membranes<sup>21,22,44–63</sup>. Simulated and experimental PXRD patterns for **(d)** C<sub>8</sub>-IL-TbBd-COF membrane, **(e)** C<sub>8</sub>-IL-TbTAPB-COF membrane, and **(f)** C<sub>8</sub>-IL-TbTTA-COF membrane. The inset is a structural formula of the corresponding amine monomer.

while the membrane thickness is further controlled through the adjustment of scraping parameters<sup>34</sup>. XRD analyses of three selections (Fig. 4a) confirm that the TbPa-COF layer grew uniformly on the surface of the polyacrylonitrile substrate (Fig. 4b). The C<sub>8</sub>-IL-TbPa-COF composite membrane has a uniform pore-size distribution of 1.3 nm and exhibits excellent sieving performance for dye molecules of different sizes (Fig. 4c,d). The nanofiltration results indicate that the C<sub>8</sub>-IL-TbPa-COF composite membrane achieves a pure water flux of 111.3 L m<sup>-2</sup> h<sup>-1</sup> bar<sup>-1</sup> and a 99.4% rejection rate for Evans Blue (EB) (Fig. 4e), thereby outperforming amorphous composite membrane (Supplementary Fig. 39). The C<sub>8</sub>-IL-TbPa-COF composite membrane demonstrates great operational stability over 72 h (Supplementary Fig. 40). Additionally, Mass balance experiments rule out the adsorption separation mechanism (Supplementary Table. 2), and Zeta

potential measurements show a negatively charged membrane surface (Supplementary Fig. 41), indicating that its nanofiltration performance mainly results from the synergistic effect of size sieving and electrostatic repulsion. The COF membrane was also applied to protein desalination using a real system named Recombinant Humanized Type I Collagen (theoretical molecular weight: 66.3 kDa). As shown in Supplementary Fig. 42, inorganic salt molecules were continuously permeated through the COF membrane, resulting in a concentrated protein solution. In practical applications (Fig. 4f and Supplementary Table. 3), a protein enrichment of 60.6% and desalination of 98.0% was achieved. In comparison, the commercially available membrane USO20 displayed a significantly lower inorganic salt permeability of only 82.6% under the same conditions (Supplementary Fig. 43 and Supplementary Table. 4).

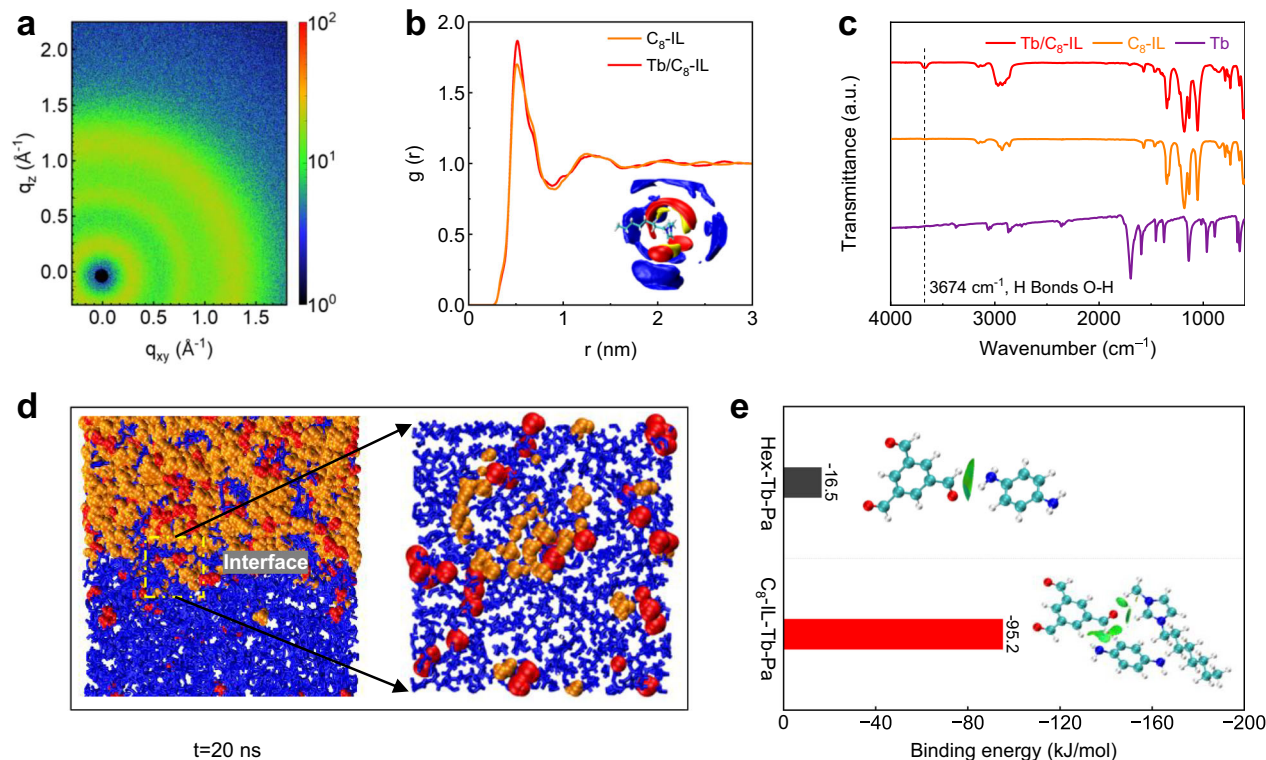


**Fig. 3 | IL/AcOH aqueous reverse-phase microemulsion interface ultrafast preparation of COF membrane reaction mechanism.** **a** 2D WAXS plots of Tb/C<sub>8</sub>-IL. **b** Radial distribution function of C<sub>8</sub>-IL and Tb/C<sub>8</sub>-IL. The inset shows the spatial distribution of the cation center of mass, the oxygen atoms (aldehyde molecule), and anion center of mass around the cation in the Tb/C<sub>8</sub>-IL system (Blue: cations, red: anions, yellow: oxygen atoms). **c** FT-IR spectra of Tb, C<sub>8</sub>-IL and Tb/C<sub>8</sub>-IL. **d** Molecular dynamics simulation of molecular structure distribution processes at

the interface of C<sub>8</sub>-IL/AcOH aqueous reverse-phase microemulsion (Blue: C<sub>8</sub>-IL (250), red: H<sub>2</sub>O (600), orange: AcOH (1200)), when  $t = 20$  ns. **e** Comparison of binding energy between Tb, Tb/C<sub>8</sub>-IL, and Pa. DFT-optimized the interaction between of Tb, Pa, and C<sub>8</sub>-IL molecules (inset). Green isosurfaces represent the intermolecular interactions quantified by an independent gradient model (isosurface = 0.001 atomic units).

## Discussion

In conclusion, we have developed a reverse-phase microemulsion interfacial polymerization approach, which can effectively achieve high-crystallinity COF membranes in seconds under mild conditions. The orderly prearrangement of aldehyde monomers and prompt encapsulation of the water by-products not only greatly promote the crystallization rate but also facilitate the oriented structure of COF membranes. This finding overcomes the perception that the preparation of high-crystallinity COF membrane requires slow crystallization and a high cost of time. This interfacial polymerization highlights great potential to efficiently prepare large-area COF membranes.

## Methods

### Chemicals and materials

Polyacrylonitrile membrane (PAN, P3500 LCD, average molecular weight cut-off: 50000 Da) was supplied by Beijing Cypriot Equipment Co. Polysulfone membrane (PSF, US020, average molecular weight cut-off: 20000 Da) was supplied by RisingSun Membrane Technology (Beijing) Co., Ltd. *p*-phenylenediamine (Pa, AR, 99%) was supplied by Sigma Aldrich (Shanghai) Trading Co., Ltd. Acetic acid (AcOH, AR, 99.5%) was supplied by Shanghai Macklin Biochemical Technology Co. 1,3,5-triformylbenzene (Tb, AR, 99%), Benzidine (Bd, AR, 95%), 1,3,5-Tris(4-aminophenyl)benzene (TAPB, AR, 98%), 4,4',4''-(1,3,5-Triazine-2,4,6-triyl)trianiline (TTA, AR, 98%), ILs (1-ethyl-3-methylimidazolium bis((trifluoromethyl)sulfonyl) imide ([C<sub>2</sub>MIm][NTf<sub>2</sub>], AR, 99%), 1-butyl-3-methylimidazolium bis((trifluoromethyl)sulfonyl) imide ([C<sub>4</sub>MIm][NTf<sub>2</sub>], AR, 99%), 1-hexyl-3-methylimidazolium bis((trifluoromethyl)sulfonyl) imide ([C<sub>6</sub>MIm][NTf<sub>2</sub>], AR, 99%), 1-octyl-3-methylimidazolium

bis((trifluoromethyl)sulfonyl) imide ([C<sub>8</sub>MIm][NTf<sub>2</sub>], AR, 99%), 1-decyl-3-methylimidazolium bis((trifluoromethyl)sulfonyl) imide ([C<sub>10</sub>MIm][NTf<sub>2</sub>], AR, 99%), 1-dodecyl-3-methylimidazolium bis((trifluoromethyl)sulfonyl) imide ([C<sub>12</sub>MIm][NTf<sub>2</sub>], AR, 99%) were purchased from Shanghai Adamas Reagent Co., Ltd. Dyes including Rose Bengal (RB, AR, 98%), Coomassie Brilliant Blue (CBB, AR, 98%), Methyl Blue (MB, BS, 98%), Amido Black 10B (AB, AR, 98%), Methyl Orange (MO, AR, 96%) and Genistein (Gs, AR, 97%) were purchased from Shanghai Macklin Biochemical Technology Co. Direct Red 80 (DR80, AR, 99%) was purchased from Shanghai Adamas Reagent Co., Ltd. Evans Blue (EB, AR, 99%) was purchased from Meryer (Shanghai) Chemical Technology Co., Ltd. Acid *p*-toluenesulfonic acid (PTSA, AR, 99%), Fuchsin (AF, AR, 99%) and Eriochrome Black T (EBT, AR, 98%) were purchased from Shanghai Aladdin Biochemical Technology, China. Methanol (AR, 99.5%) and ethanol (AR, 99.7%) were purchased from Shanghai Titan Scientific Co., Ltd. Acetone was purchased from Sichuan Xilong Scientific Co., Ltd. The BCA Protein Assay Kit was purchased from Shanghai Beyotime Biotechnology Co., Ltd. Deionized water was used for all experiments. (deionized water, Conductivity: 18.25 MΩ, filter production of Chengdu UPC deionized water machine). In this work, all chemicals and materials were used as purchased without further purification.

### Preparation of C<sub>n</sub>-IL-TbPa-COF composite membranes

Preparation of C<sub>n</sub>-IL-COF composite membranes via Scratch-assisted interface polymerization (SAIP) method. Initially, the PAN support was immersed in an amine-containing AcOH solution for 10 min to ensure thorough impregnation of both the surface and voids. Subsequently, the support was attached to a glass plate, and any excess water on the

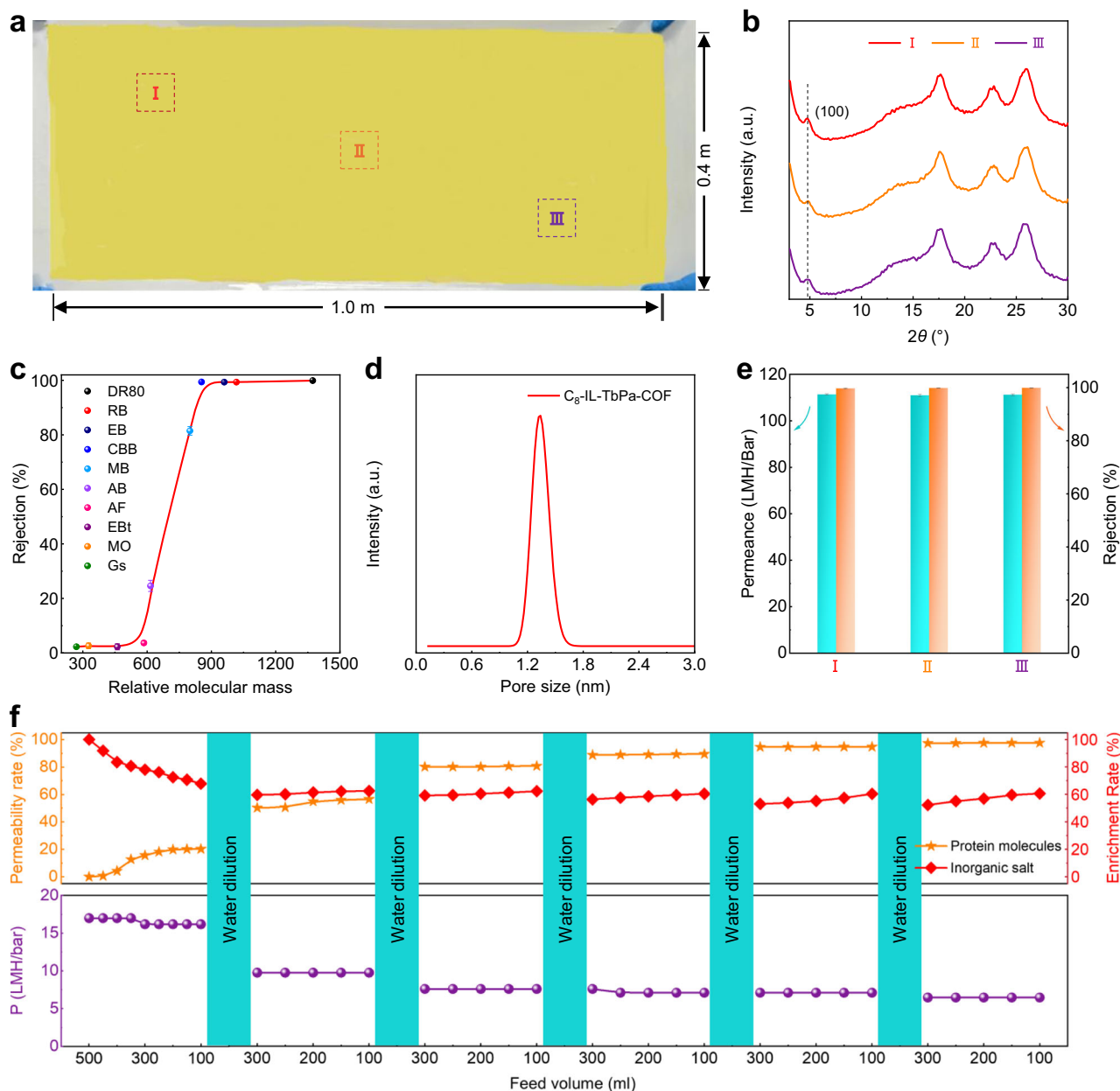


**Fig. 4 | Separation performance of the optimized  $C_8$ -IL-TbPa-COF composite membrane.** **a** Large-area  $C_8$ -IL-TbPa-COF composite membrane (0.4 × 1.0 m) fabricated by the scraping-assisted process. **b** The COF composite membrane was divided into three sections labeled I, II, III, and the sections were subsequently tested for crystallinity by XRD. Step plots of the rejection performance of COF composite membrane to various dyes were generated (**c**) and the corresponding pore-size distribution (**d**). Dyes including Direct Red 80 (DR80, MW 1373), Rose

Bengal (RB, MW 1017), Evans Blue (EB, MW 960), Coomassie Brilliant Blue (CBB, MW 854), Methyl Blue (MB, MW 800), Amido Black 10B (AB, MW 616), Acid Fuchsin (AF, MW 585), Eriochrome Black T (EBT, MW 461), Methyl Orange (MO, MW 327) and Genistein (Gs, MW 270). **e** The pure water flux and EB selectivity of the COF composite membranes in parts I, II, and III of Figure **a** were tested using a nanofiltration device. **f** COF membranes for protein desalination, changes in membrane fluxes and salt content and in protein enrichment rate the feed solution.

surface was removed using a rubber roller. An ionic liquid (IL) solution, containing 0.7 wt% of 1,3,5-triformylbenzene (Tb), was then evenly applied to the support surface in a layer of 200  $\mu$ m thickness using a scraper at a speed of 80 mm/s. Following the reaction period, any unreacted monomers present on the surface were washed away with methanol and subsequently dried in an oven for 10 minutes. The resultant membrane was then stored in deionized water for future use. By varying the type of ILs used ( $C_n$ -IL,  $n = 2, 4, 6, 8, 10, 12$ ), adjusting the concentration of AcOH in the aqueous phase ( $m$  wt%), and altering the interfacial polymerization reaction time ( $t$ ), the prepared COF membranes were designated as  $C_n$ -IL-TbPa-COF- $m$ - $t$  composite membranes.

#### Preparation of $C_n$ -IL-COF free-standing membranes

Preparation of  $C_n$ -IL-COF free-standing membranes via traditional interface polymerization method. Initially, we introduced an amine-containing 60 wt% AcOH solution to the surface of an IL solution containing 0.7 wt% Tb. Following a specified reaction period, a COF membrane formed at the IL/AcOH aqueous interface. The resultant COF membranes were subsequently washed with both methanol and acetone to eliminate any unreacted monomers from their surface. Ultimately, the membranes were stored in deionized water for future use. By utilizing various ILs ( $C_n$ -IL,  $n = 2, 4, 6, 8, 10, 12$ ) and adjusting the interfacial polymerization reaction time ( $t$  s), the prepared COF membranes were designated as  $C_n$ -IL-TbPa-COF- $m$ - $t$ s membranes.

Four COF membranes—TbPa, TbBd, TbTAPB, and TbTTA—were prepared using this method (Supplementary Figs. 44–47).

### Preparation of C<sub>8</sub>-IL-TbPa-COF composite membrane module

Initially, three C<sub>8</sub>-IL-TbPa-COF composite membranes with an effective size of 30 cm × 80 cm were fabricated. These membranes were subsequently assembled into a spiral-wound module with a feed spacer (40 × 90 cm, thickness: 0.08636 cm) and a permeate spacer (50 × 100 cm, thickness: 0.00254 cm). The module, possessing an effective area of approximately 0.7 m<sup>2</sup>, was then enclosed within a membrane shell (model 1812) for subsequent nanofiltration experiments.

### Characterization methods

Powder X-ray diffraction (PXRD) data were collected at room temperature using two different instruments, with all composite membranes analyzed on a Bruker D8 ADVANCE X-ray diffractometer (Germany) and free-standing membranes tested on a Rigaku SmartLab 9 KW X-ray diffractometer (Japan). Before analysis, samples were washed, dried, and mounted on a flat sample holder, using a high-intensity microfocus rotating anode X-ray generator with Cu K $\alpha$  radiation ( $\alpha = 1.5418 \text{ \AA}$ ) and a nickel filter. Patterns were recorded from 2° to 30° of 2 $\theta$  at a scan rate of 5° per minute, and for enhanced reliability, XRD data of all free-standing COF membranes were collected from multiple membranes. Scanning electron microscope (SEM) characterization of the surface and cross-sectional morphology of the C<sub>n</sub>-IL-TbPa-COF composite and free-standing membranes was performed using a Hitachi SU8220 SEM (Japan), with samples coated with gold for 100 s to enhance conductivity before being placed in the analysis chamber for observation. The lattice structure of C<sub>n</sub>-IL-TbPa-COF free-standing membranes was investigated using a high-resolution transmission electron microscope (HRTEM, JEOL JEM-2100F/X-Max80T, Japan), equipped with a STEM probe and an Oxford Instruments X-Max80T electrical cooling energy dispersive spectrometer system, operating at 200 kV with a point resolution of 0.23 nm and a line resolution of 0.10 nm. Fourier-transform infrared spectroscopy (FTIR) spectra were collected on a Bruker INVENIO-R spectrometer (Germany) in the 4000–600 cm<sup>-1</sup> wavenumber range. Wide angle X-ray scattering (WAXS) measurements were performed on a Xeuss 2.0 bench equipped with a copper internal source (Genix3D) producing an X-ray beam ( $\lambda = 0.15418 \text{ nm}$ , energy 8 keV), where 2D patterns were integrated into 1D intensity profiles using XCACT software as a function of scattering angle 2 $\theta$  and scattering vector  $q$  ( $q = 4\pi \sin \theta / \lambda$ ). Variable temperature WAXS data were collected using Xenocs Xeuss 3.0 HR equipment (France) with a Pilatus-300K detector and a 30 W copper target X-ray tube (wavelength 1.54189 Å), at a detector-sample distance of 400 mm, collection time of 60 seconds, and temperature range of 10–40 °C. Grazing incidence wide-angle X-ray scattering (GIWAXS) patterns were collected at beamline 19B2 in SPring-8, Japan ( $\lambda = 1.00 \text{ \AA}$ ), with images obtained at grazing angles of 0.08°, 0.12°, 0.15°, 0.30°, and 0.50° for face-on and  $\phi$ -dependent orientation distribution function (ODF) of the (001) facet. Interferometric scattering microscopy (iSCAT) equipped with a Prime 95B camera and a white light source (Hangzhou Saiman Technology Co.) was used to observe water nanoclusters in ionic liquids; prior to testing, an interface between 1 mL of 60 wt% AcOH solution and 1 mL of ionic liquid was constructed, and after a specific duration, the lower ionic liquid layer was extracted for analysis. For iSCAT testing of the IL/PTSA aqueous interface emulsion, 15.2 mg of *p*-toluenesulfonic acid (PTSA) was dissolved in 20 mL deionized water to prepare PTSA aqueous solution, IL was dried at 60 °C for 3 h with a desiccant to remove excess water, then 1 mL of IL was taken into a vial and 1 mL of PTSA aqueous was slowly added dropwise within 1 minute to form an interface layer; after standing for 10 min, the lower IL layer was taken for testing. Brunner–Emmet–Teller (BET) surface area and porosity were analyzed

via nitrogen adsorption-desorption experiments on a Micromeritics ASAP 2460 Surface Area and Porosimetry Analyzer at 393 K for activated COF membranes (C<sub>8</sub>-IL-TbPa-COF, C<sub>8</sub>-IL-TbBd-COF, C<sub>8</sub>-IL-TbTAPB-COF, and C<sub>8</sub>-IL-TbTTA-COF), with experimental pore volumes determined using the single-point adsorption model. The viscosity of six ILs was measured at 25 °C using a rotational viscometer (DV-2, Shanghai Jing Tian Electronic Instrument Co., Ltd., China) by transferring approximately 15 mL of each IL to the test cylinder equipped with a water recirculation system, fully immersing the rotor, attaching its hook to the instrument, activating the motor, and recording viscosity readings after pointer stabilization, repeating three times for each IL. High-resolution solid-state nuclear magnetic resonance (SSNMR) spectra were recorded on a Bruker 400 MHz NMR spectrometer with magic angle spinning (MAS) at 10 kHz and a 4 mm rotor. X-ray photoelectron spectroscopy (XPS) characterization of the surface elemental composition of COF membranes was performed using a Thermo Scientific K-Alpha instrument on square samples (~0.5 × 0.5 cm) fixed on the sample stage, primarily detecting C, N, O, S, and F elements. Water content in IL was measured using a Trace Moisture Analyzer (TMA, SN-WS200A) via coulometric Karl Fischer titration, where 100  $\mu$ L of IL was drawn with a microsyringe for each test and repeated three times consecutively, with the average taken as the final result.

### Nanofiltration performance and pore size distribution

The membrane permeate flux and selectivity was evaluated using a nanofiltration test device, with an effective filtration area of 7.065 cm<sup>2</sup>. The test procedure involved cutting the co-blended membrane into a circular shape that matched the inner diameter of the membrane cell and securely fixing it in the test device. Prior to testing, the membrane was pre-pressurized for one hour at an operating pressure of 4 bar. Subsequently, the total volume of solvent passing through the TbPa-COF membrane within a specified timeframe was measured. The pure water permeate flux of the membrane was then calculated using the following equation:

$$J_m = \frac{V}{A \cdot \Delta t \cdot p} \quad (1)$$

Equation (1) where  $J_m$  is the pure water flux (L·m<sup>-2</sup>·h<sup>-1</sup>·bar<sup>-1</sup>);  $V$  is the volume of permeate accumulated during the test period (L);  $A$  is the effective area of the membrane under test (m<sup>2</sup>);  $\Delta t$  is the measurement time (h); and  $p$  is the operating pressure of the membrane (bar).

The rejection rate of the membrane is calculated by the following equation.

$$R = \left(1 - \frac{C_0}{C}\right) \times 100\% \quad (2)$$

In Eq. (2):  $R$  is the rejection rate (%);  $C_0$  is the permeate concentration (mg/L);  $C$  is the feed solution concentration (mg/L).

Dye molecules with varying molecular masses served as probe molecules to evaluate the performance of the C<sub>8</sub>-IL-TbPa-COF composite membrane. A “step” plot was generated by measuring the rejection rates of dye molecules with different molecular weights, including Direct Red 80 (DR80, MW 1373), Rose Bengal (RB, MW 1017), Evans Blue (EB, MW 960), Coomassie Brilliant Blue (CBB, MW 854), Methyl Blue (MB, MW 800), Amido Black 10B (AB, MW 616), Acid Fuchsin (AF, MW 585), Eriochrome Black T (EBT, MW 461), Methyl Orange (MO, MW 327) and Genistein (Gs, MW 270). Each dyes solution was prepared at a concentration of 100 mg/L and subjected to a filtration pressure of 1 bar. Prior to testing, each feed solution was allowed to equilibrate for 1 h. The rejection rate of the C<sub>8</sub>-IL-TbPa-COF composite membranes was determined by measuring the absorbance of the permeate using an Ultraviolet-visible Spectrophotometer (U-vs).

The mean pore size distribution curve of the C<sub>8</sub>-IL-TbPa-COF composite membrane was plotted by a probability density function (PDF), which was established based on the following three assumptions: (i) There is no space and interaction between neutral substances and membrane pores. (ii) When the rejection rate is 50%, the average pore size of the DBAIP membrane is equivalent to the Stokes radius of neutral solutes. (iii) The membrane's pore size distribution is governed by the PDF.

The pore size distribution of the membrane can be expressed as follows<sup>35</sup>:

$$\frac{dR(d_p)}{dr_p} = \frac{1}{r_p \ln \sigma_p \sqrt{2\pi}} \exp \left[ -\frac{(\ln d_p - \ln \mu_p)^2}{2(\ln \sigma_p)^2} \right] \quad (3)$$

$$r_p = 16.73 \times 10^{-12} \times M_w^{0.557} \quad (4)$$

where  $\mu_p$  represents the average pore size of the membrane,  $r_p$  represents the Stokes radius of PEG solute, and  $\sigma_p$  represents the set standard deviation of PDF curve, which is defined as the ratio of the molecular radius of the solute at a rejection of 83.14% to the radius of the solute at a rejection of 50%.

### Protein desalination performance

To prepare the protein solution, dissolve 3 g of crude protein (Recombinant Humanized Type I Collagen, Theoretical molecular weight: 66.3 kDa) powder in 500 mL of deionized water. This solution is then circulated through a COF membrane, which selectively rejects the protein molecules while allowing inorganic salts to pass through. To further reduce the inorganic salt content and achieve protein concentration, the initial solution is diluted with water. The desalting process is conducted using a nanofiltration testing device, and the concentration of inorganic salts in the feed solution is measured with a conductivity meter. The protein concentration is determined using a BCA Protein Assay Kit in conjunction with a UV-2601 double-beam UV/visible spectrophotometer (Beifen-Ruili Analytical Instrument (Group) Co., Ltd.).

### Density functional theory (DFT) calculations

The geometric structures of all molecules were optimized at the B3LYP/6-311 G(d) theoretical level using Gaussian 09 software package, and frequency calculations were conducted to confirm that they represent local minima<sup>36</sup>. The optimized geometries were used to accurately calculate intermolecular interaction energies employing the B3LYP-D3(BJ)/6-311 G(d) method. Independent Gradient Model (IGM) analysis was implemented using Multiwfn software, and the visualization of weak interaction regions was achieved by combining with VMD<sup>37,38</sup>. The IGM analysis adopted Hirshfeld partitioning for electron density decomposition<sup>39</sup>, and an isosurface with an electron density of 0.001 atomic units was selected to delineate the van der Waals boundaries of the molecules, aiming to intuitively characterize the type and strength of intermolecular interactions.

### Molecular dynamic (MD) simulations

In this work, we use GROMACS (version 2022.6) program to conduct the molecular dynamic (MD) simulation for studied systems<sup>40</sup>. Packmol program was used to build the initial boxes<sup>41</sup>, all structures of simulated molecules were optimized by Gaussian 09 software (version D.01) at M062X/6-311+G\* level<sup>36</sup>, and the restrained electrostatic potential method was applied to regress the molecular charge by Multiwfn program<sup>37</sup>.

The OPLS-AA force field was selected to describe the atomic interactions<sup>42</sup>. For each MD simulation, the particle-mesh Ewald (PME) method was used to deal the long-range electrostatic interactions beyond 1.2 nm. Cutoff methods were applied for the calculation of van der Waals (vdW) interactions, with a cutoff radius set at 1.2 nm. The V-rescale thermostat and Berendsen methods were used to control temperature and pressure during the simulation process<sup>43</sup>. The simulation process comprised three stages: first, an energy minimization was conducted for 200 ps with a maximum force of 100 kJ/mol/nm between atoms. Then, an NPT simulation was conducted for 10 ns at 303.15 K and 1 atm to equilibrate the system to the desired temperature and pressure. After that, another 40 ns simulation was conducted with a time step of 1 fs using the NPT ensemble to generate the finally trajectory file for further analysis. The data from the last 10 ns were used for analysis and post-processing, such as RDF and SDF calculations.

### Data availability

All data generated or analyzed during this study are included in this published article and its supplementary information files. The data that support the findings of this study are available from the corresponding author upon request. Source data are provided with this paper.

### References

- Hu, Y. et al. Molecular recognition with resolution below 0.2 angstroms through thermoregulatory oscillations in covalent organic frameworks. *Science* **384**, 1441–1447 (2024).
- Asif, M. B., Kim, S., Nguyen, T. S., Mahmood, J. & Yavuz, C. T. Covalent organic framework membranes and water treatment. *J. Am. Chem. Soc.* **146**, 3567–3584 (2024).
- Yang, H., Xu, J. H., Cao, H., Wu, J. & Zhao, D. Recovery of homogeneous photocatalysts by covalent organic framework membranes. *Nat. Commun.* **14**, 2726 (2023).
- Li, S. et al. Direct construction of isomeric benzobisoxazole-vinylene-linked covalent organic frameworks with distinct photocatalytic properties. *J. Am. Chem. Soc.* **144**, 13953–13960 (2022).
- Hao, Q. et al. Oriented two-dimensional covalent organic framework films for near-infrared electrochromic application. *J. Am. Chem. Soc.* **141**, 19831–19838 (2019).
- Wang, K. et al. Monolayer-assisted surface-initiated schiff-base-mediated aldol polycondensation for the synthesis of crystalline sp<sup>2</sup> carbon-conjugated covalent organic framework thin films. *J. Am. Chem. Soc.* **145**, 5203–5210 (2023).
- Bag, S. et al. Covalent organic framework thin-film photodetectors from solution-processable porous nanospheres. *J. Am. Chem. Soc.* **145**, 1649–1659 (2023).
- Zuo, P. et al. Near-frictionless ion transport within triazine framework membranes. *Nature* **617**, 299–305 (2023).
- Zuo, X. et al. Thermo-osmotic energy conversion enabled by covalent-organic-framework membranes with record output power density. *Angew. Chem. Int. Ed.* **61**, e202116910 (2022).
- Xu, J. et al. An olefin-linked covalent organic framework as a flexible thin-film electrode for a high-performance micro-supercapacitor. *Angew. Chem. Int. Ed.* **58**, 12065–12069 (2019).
- Yang, Y. et al. Elastic films of single-crystal two-dimensional covalent organic frameworks. *Nature* **630**, 878–883 (2024).
- Zhang, W. et al. Reconstructed covalent organic frameworks. *Nature* **604**, 72–79 (2022).
- Zhou, Z. et al. Growth of single-crystal imine-linked covalent organic frameworks using amphiphilic amino-acid derivatives in water. *Nat. Chem.* **15**, 841–847 (2023).
- Tang, J. Q. et al. Large-area free-standing metalloporphyrin-based covalent organic framework films by liquid-air interfacial

- polymerization for oxygen electrocatalysis. *Angew. Chem. Int. Ed.* **62**, e202214449 (2023).
15. Fan, C. Y. et al. Scalable fabrication of crystalline COF membranes from amorphous polymeric membranes. *Angew. Chem. Int. Ed.* **60**, 18051 (2021).
  16. Sasmal, H. S., Kumar Mahato, A., Majumder, P. & Banerjee, R. Landscaping covalent organic framework nanomorphologies. *J. Am. Chem. Soc.* **144**, 11482–11498 (2022).
  17. Emmerling, S. T. et al. In situ monitoring of mechanochemical covalent organic framework formation reveals templating effect of liquid additive. *Chem* **7**, 1639–1652 (2021).
  18. Guan, Q., Zhou, L. L. & Dong, Y. B. Construction of covalent organic frameworks via multicomponent reactions. *J. Am. Chem. Soc.* **145**, 1475–1496 (2023).
  19. Du, J. et al. Ultrafast interfacial self-assembly toward bioderived polyester COF membranes with microstructure optimization. *Adv. Mater.* **36**, 2405744 (2024).
  20. Karak, S., Kumar, S., Pachfule, P. & Banerjee, R. Porosity prediction through hydrogen bonding in covalent organic frameworks. *J. Am. Chem. Soc.* **140**, 5138–5145 (2018).
  21. Dey, K. et al. Selective molecular separation by interfacially crystallized covalent organic framework thin films. *J. Am. Chem. Soc.* **139**, 13083–13091 (2017).
  22. Matsumoto, M. et al. Lewis-acid-catalyzed interfacial polymerization of covalent organic framework films. *Chem.* **4**, 308–317 (2018).
  23. Du, J. et al. A 2D soft covalent organic framework membrane prepared via a molecular bridge. *Adv. Mater.* **35**, 2300975 (2023).
  24. Kandambeth, S. et al. Selective molecular sieving in self-standing porous covalent-organic-framework membranes. *Adv. Mater.* **29**, 1603945 (2016).
  25. Ma, T. et al. Single-crystal x-ray diffraction structures of covalent organic frameworks. *Science* **361**, 48–52 (2018).
  26. Han, J. et al. Fast growth of single-crystal covalent organic frameworks for laboratory x-ray diffraction. *Science* **383**, 1014–1019 (2024).
  27. Ding, S. Y. et al. Construction of covalent organic framework for catalysis: Pd/COF-LZU1 in Suzuki–Miyaura coupling reaction. *J. Am. Chem. Soc.* **133**, 19816–19822 (2011).
  28. Deng, L. et al. Ionic liquid-accelerated growth of covalent organic frameworks with tunable layer-stacking. *Angew. Chem. Int. Ed.* **63**, e202408453 (2024).
  29. Wang, Y. et al. Insights into ionic liquids: from Z-bonds to Quasi-liquids. *JACS Au* **2**, 543–561 (2022).
  30. Wang, Y. L. et al. Microstructural and dynamical heterogeneities in ionic liquids. *Chem. Rev.* **120**, 5798–5877 (2020).
  31. Hayes, R., Warr, G. G. & Atkin, R. Structure and nanostructure in ionic liquids. *Chem. Rev.* **115**, 6357–6426 (2015).
  32. Wu, Y. et al. Crystallizing self-standing covalent organic framework membranes for ultrafast proton transport in flow batteries. *Angew. Chem. Int. Ed.* **62**, e202313571 (2023).
  33. Dupont, J. et al. Ionic liquids in metal, photo-, electro-, and (bio) catalysis. *Chem. Rev.* **124**, 5227–5420 (2024).
  34. Pan, Y. et al. Membranes based on covalent organic frameworks through green and scalable interfacial polymerization using ionic liquids for antibiotic desalination. *Angew. Chem. Int. Ed.* **63**, e202316315 (2024).
  35. Wu, B., Wang, N., Shen, Y., Jin, C. G. & An, Q. F. Inorganic salt regulated zwitterionic nanofiltration membranes for antibiotic/monovalent salt separation. *J. Membr. Sci.* **666**, 121144 (2023).
  36. Zhao, Y. & Truhlar, D. G. The M06 suite of density functionals for main group thermochemistry, thermochemical kinetics, non-covalent interactions, excited states, and transition elements: two new functionals and systematic testing of four M06-class functionals and 12 other functionals. *Theor. Chem. Acc.* **120**, 215–241 (2007).
  37. Lu, T. A comprehensive electron wavefunction analysis toolbox for chemists, Multiwfn. *J. Chem. Phys.* **161**, 42 (2024).
  38. Lu, T. & Chen, F. Multiwfn: a multifunctional wavefunction analyzer. *J. Comput. Chem.* **33**, 580–592 (2011).
  39. Lu, T. & Chen, Q. Independent gradient model based on Hirshfeld partition: a new method for visual study of interactions in chemical systems. *J. Comput. Chem.* **43**, 539 (2022).
  40. Van Der, D. S. et al. GROMACS: fast, flexible, and free. *J. Comput. Chem.* **26**, 1701–1718 (2005).
  41. Martínez, L., Andrade, R., Birgin, E. G. & Martínez, J. M. PACKMOL: a package for building initial configurations for molecular dynamics simulations. *J. Comput. Chem.* **30**, 2157–2164 (2009).
  42. Jorgensen, W. L., Maxwell, D. S. & Tirado-Rives, J. Development and testing of the OPLS all-atom force field on conformational energetics and properties of organic liquids. *J. Am. Chem. Soc.* **118**, 11225–11236 (1996).
  43. Berendsen, H. J. C., Postma, J. P. M., van Gunsteren, W. F., DiNola, A. & Haak, J. R. Molecular dynamics with coupling to an external bath. *J. Chem. Phys.* **81**, 3684–3690 (1984).
  44. Wang, G. et al. Rapid synthesis of self-standing covalent organic frameworks membrane via polyethylene glycol-assisted space-confined strategy. *J. Membr. Sci.* **652**, 120494 (2022).
  45. Wang, R. et al. Ultrathin covalent organic framework membranes prepared by rapid electrophoretic deposition. *Adv. Mater.* **34**, 2204894 (2022).
  46. Hao, S., Zhang, T., Fan, S., Jia, Z. & Yang, Y. Preparation of COF-TpPa1 membranes by chemical vapor deposition method for separation of dyes. *Chem. Eng. J.* **421**, 129750 (2021).
  47. Fang, Y.-X., Lin, Y.-F., Xu, Z.-L., Mo, J.-W. & Li, P.-P. A novel clover-like COFs membrane fabricated via one-step interfacial polymerization for dye/salt separation. *J. Membr. Sci.* **673**, 121470 (2023).
  48. Liu, D. et al. Moderately crystalline azine-linked covalent organic framework membrane for ultrafast molecular sieving. *ACS Appl. Mater. Interfaces* **13**, 37775–37784 (2021).
  49. Wang, M. et al. Electrochemical interfacial polymerization toward ultrathin COF membranes for brine desalination. *Angew. Chem. Int. Ed.* **62**, e202219084 (2023).
  50. Hao, S., Jiang, L., Li, Y., Jia, Z. & Van der Bruggen, B. Facile preparation of COF composite membranes for nanofiltration by stoichiometric spraying layer-by-layer self-assembly. *Chem. Commun.* **56**, 419–422 (2020).
  51. Khan, N. A. et al. Solid-vapor interface engineered covalent organic framework membranes for molecular separation. *J. Am. Chem. Soc.* **142**, 13450–13458 (2020).
  52. Wu, Y. et al. Solvent-induced interfacial polymerization enables highly crystalline covalent organic framework membranes. *J. Membr. Sci.* **659**, 120799 (2022).
  53. Pantano, M. F. et al. Large freestanding 2D covalent organic framework nanofilms exhibiting high strength and stiffness. *Mater. Today Chem* **26**, 101007 (2022).
  54. Yang, Y., Li, G., Ouyang, D., Cai, Z. & Lin, Z. Dual-activation interfacial polymerization based anionic covalent organic framework nanofiltration membrane for high-flux dye separation. *Chem. Eng. J.* **456**, 141008 (2023).
  55. Shinde, D. B. et al. Pore engineering of ultrathin covalent organic framework membranes for organic solvent nanofiltration and molecular sieving. *Chem Sci* **11**, 5434–5440 (2020).
  56. Chen, J. et al. Surfactant-assisted interfacial polymerization towards high-crystallinity COF membranes for organic solvent nanofiltration. *J. Membr. Sci.* **694**, 122404 (2024).
  57. Shinde, D. B. et al. Crystalline 2D covalent organic framework membranes for high-flux organic solvent nanofiltration. *J. Am. Chem. Soc.* **140**, 14342–14349 (2018).
  58. Sheng, F. et al. Cationic covalent organic framework membranes for efficient dye/salt separation. *J. Membr. Sci.* **644**, 120118 (2022).

59. Wang, H. et al. Brønsted acid mediated covalent organic framework membranes for efficient molecular separation. *J. Mater. Chem. A* **7**, 20317–20324 (2019).
60. Zhu, T. et al. 3D covalent organic framework membrane with fast and selective ion transport. *Nat. Commun.* **14**, 5926 (2023).
61. Shen, J. et al. Polydopamine-modulated covalent organic framework membranes for molecular separation. *J. Mater. Chem. A* **7**, 18063–18071 (2019).
62. Gao, S. et al. The ionic liquid-H<sub>2</sub>O interface: a new platform for the synthesis of highly crystalline and molecular sieving covalent organic framework membranes. *ACS Appl Mater Interfaces* **13**, 36507–36516 (2021).
63. Cao, L. et al. Switchable Na<sup>+</sup> and K<sup>+</sup> selectivity in an amino acid functionalized 2D covalent organic framework membrane. *Nat. Commun.* **13**, 7894 (2022).

## Acknowledgements

This work was financially supported by the National Natural Science Foundation of China (U23A20688, H.M., and 22468046, W.H.Z.). Partial support from Robert A. Welch Foundation (B-0027, S.Q.M.) is also acknowledged. The synchrotron radiation experiments were performed at BL19B2 of SPring-8 with the approval of the Japan Synchrotron Radiation Research Institute (JASRI) (Proposal Nos. 2024B1657 and 2025A1540).

## Author contributions

Conceptualization: Y.P., W.H.Z., H.M. Supervision: W.H.Z., H.M. Membrane fabrication: Y.P. Characterization and performance tests: Y.P., L.T.G., X.Y.L., T.F.W. DFT calculation and MD simulations: G.Q.Y., L.Y., H.Q.G. Result analysis: Y.P., W.H.Z., H.M. Writing—original draft: Y.P. Writing—review & editing: Y.P., W.H.Z., S.Q.M., H.M.

## Competing interests

The authors declare no competing interests.

## Additional information

**Supplementary information** The online version contains supplementary material available at <https://doi.org/10.1038/s41467-025-67569-9>.

**Correspondence** and requests for materials should be addressed to Wenhai Zhang, Shengqian Ma or Hong Meng.

**Peer review information** *Nature Communications* thanks Congcong Yin, Dan Zhao and the other, anonymous, reviewer(s) for their contribution to the peer review of this work. A peer review file is available.

**Reprints and permissions information** is available at <http://www.nature.com/reprints>

**Publisher's note** Springer Nature remains neutral with regard to jurisdictional claims in published maps and institutional affiliations.

**Open Access** This article is licensed under a Creative Commons Attribution-NonCommercial-NoDerivatives 4.0 International License, which permits any non-commercial use, sharing, distribution and reproduction in any medium or format, as long as you give appropriate credit to the original author(s) and the source, provide a link to the Creative Commons licence, and indicate if you modified the licensed material. You do not have permission under this licence to share adapted material derived from this article or parts of it. The images or other third party material in this article are included in the article's Creative Commons licence, unless indicated otherwise in a credit line to the material. If material is not included in the article's Creative Commons licence and your intended use is not permitted by statutory regulation or exceeds the permitted use, you will need to obtain permission directly from the copyright holder. To view a copy of this licence, visit <http://creativecommons.org/licenses/by-nc-nd/4.0/>.

© The Author(s) 2025